Quantification of Nanoscale Density Fluctuations in Biological Cells/Tissues: Inverse Participation Ratio (IPR) Analysis of Transmission Electron Microscopy Images and Implications for Early-Stage Cancer Detection

Prabhakar Pradhan[1], Dhwanil Damania[1], Hemant K. Roy[2], Hrushikesh Joshi[3], Allen Taflove[4], Vinayak Dravid[3], Vadim Backman[1]

[1]Biomedical Engineering Department, Northwestern University, Evanston, IL 60208, USA,
[2]Department of Internal Medicine, NorthShore University HealthSystem, Evanston, IL 60208, USA
[3]Department of Material Science and Engineering, Northwestern University, Evanston, IL 60208, USA
[4]Department of Electrical Engineering and Computer Science, Northwestern University, Evanston, IL 60208, USA
Correspondence should be addressed to P.P.; email: pradhan@northwestern.edu

Most cancers are curable if they are diagnosed and treated at an early stage. Recent studies suggest that there are nano-architectural changes occurring within cells during early carcinogenesis which precede microscopically evident tissue changes. It follows that the ability to comprehensively interrogate cell nanoarchitecture (e.g., length scale of macromolecular complexes, DNA, RNA, proteins, and lipid membranes) could be critical to study early carcinogenesis. We report a study of the nanoscale mass density fluctuations of biological cells and tissues by quantifying their nanoscale light-localization properties. Transmission electron microscope (TEM) images of human colon cancer cell line (HT29) variants and tissues are used to construct corresponding effective disordered optical lattices. Light-localization properties are studied by statistical analysis of the inverse participation ratio (IPR) of the eigenfunctions of these optical lattices at the nanoscales. First, the IPR analysis is validated in experiments with models of disordered systems fabricated from dielectric nanoparticles. Second, our experimental results from genetically modified HT29 cell line variants show a statistically significant increase of the average IPR value, which parallels the genetic events leading to an increase in the aggressive growth of these cell lines. A similar trend of the IPR values is confirmed in human tissues in patients with an early stage colon neoplasia. These results indicate

elevation of the nanoscale disorder strength (refractive index fluctuations) in early carcinogenesis. Importantly, our results demonstrate that the increase in the nanoscale disorder represents the earliest structural alteration in cells undergoing carcinogenesis known to-date.

Cancer is one of the leading causes of death in the United States and worldwide (1). Cell morphology, from molecular to cellular levels, is inherently linked to biochemical, biomechanical and transport processes within the cell. Examples include the effects of high-order chromatin structure on gene transcription and genetic information flow in the nucleus (2,3,4,5), macromolecular crowding on the cytoskeletal biomechanical properties and protein folding in the cytoplasm (6,7,8,9) **.** Although significant body of knowledge regarding genetic and epigenetic alterations in carcinogenesis has been accumulated, structural intracellular changes are still incompletely understood. Conventional visible-light microscopy techniques allow detection of morphological changes at the micron and supramicron scales in tissues/cells that are prominent in the later stages of carcinogenesis (i.e. dysplasia) resulting from multiple genetic and epigenetic alterations (10,11,12,13). However, understanding the earlier initiating morphological events in carcinogenesis would require the ability to detect nanoarchitectural changes, which, at best, remains challenging. In particular, the ability to comprehensively interrogate the nanoarchitecture of single cells and tissues is critical for applications that require an understanding of the role of cell nanoarchitecture in early carcinogenesis (5) (14). To date, however, the nanoarchitectural properties of cells/tissues have not been either well understood or studied.

As suggested by several recent studies, the progression of cancer in early stages is accompanied by nanoscale morphological or architectural changes in the internal cell structure prior to histological abormalities. Such changes result in mass-density fluctuations in cells, also on the nanoscale. Conventional visible-light microscopy techniques have been widely used to characterize biological systems, but their ability to detect changes at the nanoscale is fundamentally impeded by their diffraction-limited resolution (15). However, recent spectral-dependent optical microscopy studies have shown that such nanoscale fluctuations are prominent in early carcinogenesis (16,17,18). Furthermore, these studies indicate that changes in molecular morphology occur at length scales of approximately 10 nm to 100 nm, which

reflect the cellular building blocks (e.g., DNA, RNA, proteins and lipids). However, optical techniques are unable to probe the detailed nature of these nanoscale changes. This obstacle led us to study transmission electron microscope (TEM) imaging, which enables both quantitative and qualitative assessments of nanoarchitectural changes in the early stages of carcinogenesis. Specifically, the nanoscale resolution of TEM imaging has allowed us to make a quantitative assessment of cellular nanoarchitectural information via their mass-density measurement.

TEM imaging techniques have been widely used to visualize nano- and micro-structures in biological samples (19). However, the quantitative information embedded within a TEM grayscale image is poorly understood — in particular, subtle short-range nanoscale fluctuations and correlations of the grayscale, and the changes of such fluctuations with disease (20).

In this paper, we report for the first time the quantification of nanoscale mass-density fluctuations in human colon cancer cell lines and tissues by studying their light-localization properties via TEM image analysis. To accomplish this, we borrowed an idea from condensed-matter physics and applied it for the first time to a biological system. In brief, this concept involves first constructing optical lattices from the optical mass-density fluctuations, and then studying the optical-localization properties of these lattices. The high resolution of TEM imaging allows investigation of nanoscale fluctuations of the mass densities of thin slices (~10-100 nm) of tissue samples (19). The TEM images from human cells and tissues are projected to their corresponding effective optical lattices via the construction of their effective biological mass densities. The optical eigenfunctions of these lattices are then obtained (detailed in Sec. II). The inverse participation ratio (IPR) of an eigenfunction E is defined as $IPR = \int |E(r)|^4 \, d\vec{r}$ (in units of inverse area). The statistical properties of IPR (or light-localization properties) are important quantitative measures of the localization of light in an optical lattice (ordered or disordered). Note that the average value of *IPR* for a uniform lattice is a fixed universal number (approximately 2.5); and that the IPR value increases from a uniform lattice to a disordered lattice with the increase in the degree of the disorder or transport mean free path. This has been well studied in condensed-matter physics for characterizing the disorder properties of localization and the quantum Hall effect (21,22,23,24).

In the discussion to follow, we first demonstrate the validity of applying IPR analyses to measure nanoscale disorder and mass-density fluctuations. Specifically, we review our

laboratory TEM calibration experiments on canonical systems of dielectric nanoparticles deposited on dielectric thin films. These experiments quantified the changes in the nanoscale disorder strength of a sample using the IPR technique upon systematically varying the disorder or the mass density of the nanoparticles in the sample.

Then, we report the results of applying IPR analyses to laboratory experiments studying the correlation of mass-density fluctuations with the degree of aggressive growth of a cancer cell. These experiments involved the HT29 human colon cancer cell line and its genetic variant which exhibits even more aggressive growth or proliferation: tumor-suppressor c-terminus sarc kinase-knockdown (CSK) HT29 cells (25). We find that the IPR properties of the CSK cells are statistically different than those of the HT29 cells.

Finally, we report the results of applying IPR analyses to study changes in the mass-density fluctuations of rectal mucosa tissues from patients having adenomatous polyps located in the colon (26,27). Data from these studies are compared to corresponding rectal-tissue data from normal patients. We find that the IPR properties of rectal tissues located in the field of precancerous colonic adenomas are statistically significantly different than the IPR properties of rectal tissues from healthy individuals .

Results

I. Quantification of nanoscale mass-density fluctuations of dielectric nanoparticles on dielectric thin films

(i) Sample preparation

In order to investigate the hypothesis that IPR can accurately quantify nanoscale disorder changes, we performed TEM studies on model experimental samples/systems of dielectric nanoparticles (~6 nm) deposited on formvar dielectric thin films. The formvar thin film provides a base sample or a nearly uniform background, while the deposited dielectric nanoparticles act as a disordered medium comprised of nanoscatterers.

While much simpler than a biological system, this model allows control and characterization of the disorder strength. Both have an average uniform refractive index background (n_0) and weaker refractive index fluctuations (Δn) above the uniform background ($\Delta n/n_0 << 1$).

The sample preparation procedure for the model system, i.e. nanoparticles on a dielectric thin film, is described in detail in Section V: Methods. A copper mesh was placed above the formvar thin film, and nanoparticles in a hexane solution of fixed concentration were spread over the mesh on the thin film. Then, the sample was ultra-sonicated (see Methods) to achieve as random as possible a distribution of the nanoparticles on the thin film, and to avoid formation of a lattice structure of the nanoparticles due to van der Waals interactions. Finally, the nanoparticle solution was allowed to dry on the film. Subsequently, TEM micrographs were obtained (Joel 2002, TEM machine) for each of the prepared samples having varying concentrations of nanoparticles on the thin films. A 200 keV electron beam with a fixed magnification (40K) was used for each micrograph.

The goal of this experiment was to determine if the short-length-scale disorder strength can be measured by the IPR technique, and how the value of average IPR changes with an increase in the nanoscale density or the mean free path. A short portion of a TEM micrograph is shown in Figure 1 (top, left), and the discretization of the TEM grayscale image, i.e. a lattice image with varying intensity, is shown in Figure 1 (top, right).

(ii) Projection of TEM images onto optical lattices and the IPR calculation

The TEM grayscale intensity I_{TEM} decays exponentially with the thickness of the sample for a thin sample, where the decay constant is a function of the mass density (10). This exponential decay can be approximated as a linear decay for a very thin sample. TEM studies of thin layers of nanoscale dielectric beads have shown that I_{TEM} is linearly proportional to the mass density of the beads (28,29). For a very-thin dielectric/biological sample, we have assumed that the grayscale TEM image intensity at any lattice point, $I_{\mathrm{TEM}}(x, y)$ (Figs.1(a), 1(b), 1(c)), is linearly proportional to the total mass, $M(x, y)$ (total biomass for biological samples) present in the corresponding dielectric film/tissue voxel around the lattice point (dimensions: 10 nm × 10 nm in the x-y plane, 70 nm along the z-direction) of the tissue slices.

However, we stress here that the exact functional form is not important for our present analyses. Our only requirement is that the changes of the dielectric constants are analytic around the mean value. Note that, in case of biological samples, the constructed optical lattice is an effective lattice for the sample in the presence of contrast agent used during sample

preparation process of the TEM imaging (see Methods). Therefore, we further consider that for biological samples, absorption of the contrast agent by the thin tissue voxel is also linearly proportional to the total mass present in the voxel.

Assuming that the refractive index $n(x, y)$ of a voxel is functionally proportional to its biomass, we can write:

$$n(x, y) = f(M(x, y)) = f(I_{\mathrm{TEM}}(x, y)) \tag{1}$$

We assume that the form of I_{TEM} is given by

$$I_{\mathrm{TEM}}(x, y) = I_0 + \Delta I_{\mathrm{TEM}}(x, y) \tag{2}$$

where I_0 is the mean background of the whole TEM sample, and $\Delta I_{\mathrm{TEM}}(x, y)$ is the fluctuating part of the intensity around a point (x, y) of the pixel. Then, the refractive index of a tissue voxel from the corresponding TEM pixel can be written as

$$n(x, y) = n_0 + \Delta n(x, y) = f(I_{\mathrm{TEM}}(x)) = f_0 + f_0' \times \Delta I_{\mathrm{TEM}}(x, y) \tag{3}$$

where n_0 is the constant-background part of the full sample, and $\Delta n(x, y)$ is the fluctuating part of the refractive index in the pixel of the constructed optical lattice. It can be shown that the effective optical potential of an optical lattice ε_i has the following form (20)(30):

$$\varepsilon_i \propto \Delta n(x, y) / n_0 = (\Delta I_{\mathrm{TEM}}(x, y) / I_0) \times (I_0 \times f_0' / f_0) \tag{4}$$

where $\Delta I_{\mathrm{TEM}}(x, y) << I_0$ and $\Delta n(x, y) << n_0$ (e.g., for tissue, n_0 = 1.33–1.38, and Δn = 0.01–0.1) (31). We then calculated the exact eigenfunctions ($E_i(x, y)$, i = *1–N*) of each two-dimensional pixel of optical sample size $L \times L$ by solving the wave equation for the electric field in the lattice using a disorder tight-binding model (32,33).

(iii) Tight-binding model construction:

To quantify the disorder properties of the TEM images, we have carried out numerical calculations of the Anderson disorder tight-binding model (TBM). The TBM has been well studied, and has proven to be a good model for describing single-electron states or localized optical states of systems of any geometry and disorder. We consider one optical state of a photon per lattice site, and the interlattice site hoppings are restricted to the nearest neighbors only. Such a Hamiltonian can be written as (32,33).

$$H = \sum_i \varepsilon_i |i\rangle\langle i| + t \sum_{<i\,j>} |i\rangle\langle j| + |j\rangle\langle i| \tag{5}$$

where $\varepsilon_i \propto \Delta n(x,y)/n_0$ is the i^{th} lattice site energy; $|i\rangle$ and $|j\rangle$ are the optical wavefunctions at the i^{th} and j^{th} lattice sites, respectively; $<i\ j>$ indicates the nearest neighbors; and t is the overlap integral between sites i and j.

In our analyses, for short-length refractive index fluctuations, a large TEM micrograph of 15.8 μm × 15.8 μm (as shown in Figs. 1(a) and 1(b)) is virtually cut into smaller 77 nm × 77 nm to 308 nm × 308 nm samples or IPR pixels. To project the TEM image to the tight-binding model, first the fluctuating part of every grayscale point of the TEM image is considered as proportional to the onsite optical potential energy ε_i (i.e., Eq. (3)). The optical potential ε_i is then rescaled such that its mean is the same as the hopping parameter, i.e. t = mean(ε_i), and we further consider $(I_0(x,y) f_0'/ f_0)/t = constant$ =1 without any loss of generality. We define the sample length as L (in nm), the lattice size as L_a units (dimensionless), and the unit lattice length as a (in nm) such that $L = L_a \times a$. The eigenfunctions of each pixel of size $L \times L$ are then calculated. The average value of the IPR of an IPR pixel can then be written as (21,22,23):

$$< IPR(L) >_{\text{Pixel}} = \frac{1}{N} \sum_{i=1}^{N} \int_0^L \int_0^L E_i^4(x,\, y)\, dx\, dy \tag{6}$$

where E_i is the i^{th} eigenfunction of the Hamiltonian in Eq.(5) of an optical lattice (i.e. an IPR pixel) of size $L \times L$; $N = L_a^2$ ($L_a = L/a$, $a = dx = dy$) is the total number of the eigenfunctions;

and $< >_{\text{Pixel}}$ denotes averaged over all the N eigenfunctions of the IPR pixel. By the construction of each IPR pixel, we are mainly considering the fluctuating part of n relative to its average background as the rescaled potential.

(iv) Statistical analyses of IPR studies of TEM images

Figures 1*A*, 1*B*, and 1*C* show the representative TEM grayscale images (micrographs) of three different concentrations of the nanoparticles on dielectric formavare bases. To illustrate the potential of the IPR technique in distinguishing minute differences in disorder strength, we have studied length-scale dependence statistical properties of the IPR pixels at the nanoscales (50 nm × 50 nm) to (400 nm × 400 nm). Approximately 5 to 8 TEM images were analyzed for each sample type of similar concentration of nanoparticles.

Figures 1*D*, 1*E*, and 1*F* show the corresponding IPR pixel images (pixel size = 154 nm × 154 nm, i.e., lattice size = 20 × 20). Figures 1*G*, 1*H*, and 1*I* show the $\text{IPR}_{\text{Pixel}}$ distributions corresponding to Figs. 1*D*, 1*E*, and 1*F*. These clearly show that the IPR values increase with an increase of the concentration of the nanoparticles (disorder strength).

Figure 1*J* shows the $< IPR(L) >_{\text{Pixel}}$ values for the different length scales, with respect to the uniform background, of three types of TEM micrographs for three different concentrations of nanoparticles.

The average of the $\text{IPR}_{\text{Pixel}}(L)$ increases with the sample (i.e., lattice) size. This indicates the increase of the nanoscale disorder strength due to the increase of the nanoscale mass density fluctuations, and is consistent with the IPR theory. Overall, the validation study of Fig. 1 shows that nanoscale disorder can be quantified by the IPR technique, which can distinguish statistically significant differences between two disordered systems. This example is one of the simplest possible model systems, i.e. a dielectric background with dielectric nanoparticles. However, the properties are relevant for any other disordered dielectric media. The trend would be same but the actual values may be different.

In the next Section, we will apply the above validated idea for the IPR technique to study the disorder strength of biological cells and their changes during cancerous growth.

II. Nanoscale mass-density fluctuation analysis of HT29 cells and their CSK genetic variant

(i) HT29 cell line and its genetic variance CSK

Recently, we reported a partial-wave spectroscopic (PWS) microscopic technique which demonstrated that the optical disorder strength due to nanoscale refractive-index fluctuations is significantly higher for CSK cells than that of the HT29 control (16,17,18). However, optical measurements did not show the exact nature of the changes within these cells. In the present work, we applied TEM with the goal of more rigorously investigating the nature of the nanoscale fluctuations indicated by our prior PWS studies.

To investigate the hypothesis that nanoscale mass-density fluctuations increase with cancerous growth (as seen in our prior PWS optical experiments), we performed experiments on the well-characterized HT29 cell line and its CSK variant engineered via ShRNA to have a CSK knockdown that exhibits more aggressive growth. HT29 (control) cells are human colonic adenocarcinoma cells that are able to express differentiation features which are characteristic of mature colonic cells. The knockdown of the tumor-suppressor CSK gene increases the growth/proliferation of the HT29 cells. In our TEM experiments with these cells, we were interested to observe the effect of aggressive cancerous growth on intracellular mass-density fluctuations at the nanoscale. We note that all of these cells are cytologically (and hence microscopically) indistinguishable.

(ii) Cell Sample Preparation for TEM imaging

In our experiment, HT29 cells were stably transfected with ShRNA plasmid or empty vector control. The knockdown of the tumor-suppressor CSK gene increases the growth of the HT29 cells. The HT29 cells were cultured in the laboratory, and the preparation of the CSK genetic variation of the HT29 cells was performed according to a standard protocol as described in Methods.

Both HT29 and CSK cells underwent the same sample preparation protocol for TEM imaging: fixation, staining, embedding, sectioning, and finally TEM imaging, as per standard protocols described in Methods.

(iii) IPR analysis of the TEM images of the HT29 and CSK cells

Figures 2*A* and 2*B* show the representative TEM grayscale images of HT29 cells and their more aggressive genetic variant, CSK cells. The corresponding IPR images (IPR-pixel by pixel, IPR pixel dimension = 154 nm × 154 nm, i.e., lattice size = 20 × 20) are shown in Figs. 2*C* and 2*D*. The IPR images of two cells clearly indicate two different states of disorder.

To illustrate the potential of the IPR technique in detecting the difference in the nanoscale fluctuations between these cytologically indistinguishable cell types, we calculated the ensemble-averaged properties of the IPR of both the HT29 and CSK cell types. Five TEM images from each type of cell were analyzed (a total of ten TEM images of the cell). Each TEM micrograph dimension is 15.8 μm × 15.8 μm, and the corresponding lattice size is 1048 × 1048 pixels.

Figure 2*E* shows the $< IPR(L) >_{\text{Pixel}}$ distributions of representative HT29 and CSK cells for IPR pixel sizes: $L \times L$ = 154 nm × 154 nm (i.e., lattice sizes ($L_a = L/a$, a = 7 nm), $L_a \times L_a$ = 20 × 20). This illustrates a distinct separation in nanoscale fluctuation between the two types of cells. The average and the standard deviation of the distribution both increase for the CSK cells relative to HT29 cells.

Figure 2*E* (inset) shows the standard deviation $\sigma(< IPR(L) >_{\text{Pixel}})$ versus L plot for the CSK cells relative to the HT29 cells. The $\sigma(< IPR(L) >_{\text{Pixel}})$ and $<< IPR(L) >_{\text{Pixel}}>$ both increase with increasing L for the CSK cells relative to the HT29 cells, indicating a relatively greater disorder for the CSK cells. The p-values are

Figure 2*F* shows $<< IPR(L) >_{\text{Pixel}}>$ versus L plots for three different cases: (i) uniform lattice; (ii) HT29 cells; and (iii) CSK cells. The ensemble averaging is denoted by < >, and was performed over 50,000 IPR pixels for the length scale L = 77 nm (i.e., L_a = 10) and over 3,125 IPR pixels for pixel length L = 308 nm (i.e., L_a = 40) for each type of cells. The three curves in Fig. 2*F* clearly show that the $<< IPR(L) >_{\text{Pixel}}>$ value is higher for CSK cells relative to HT29 cells. For example, $<< IPR(L) >_{\text{Pixel}}>$ values for the uniform background, HT29 cells, and CSK cells are 2.5, 2.8259, and 2.9978, respectively. (Student *t*-test, two-tailed *p*-value = 4.36×10^{-12}).. The higher value of the average IPR corresponds to the higher disorder strength due to the larger nanoscale fluctuations in the optical lattices.

III. Nanoscale mass-density fluctuation of normal and early precancerous colon tissues

As discussed in the previous two sections, we determined that the IPR technique permits measuring changes in nanoscale mass-density fluctuations. Furthermore, in the context of HT29 and CSK human colon cancer cells, we found that these nanoscale fluctuations increase with more aggressive growth. Based on the above results, we subsequently investigated whether the IPR technique is applicable in early carcinogenesis or not? To evaluate this, we looked at Field effect as a manifestation of it.

To this end, we carried out a pilot human study involving IPR analysis of a total of 100 TEM images of rectal tissues: 50 TEM images from a group of patients previously determined to have no colonic dysplasia; and 50 TEM images from a group of early precancerous patients having microscopically normal rectal tissues. Each TEM micrograph spanned 15.8 μm × 15.8 μm, and the corresponding lattice size was 2048 pixels × 2048 pixels.

(i) Tissue sample preparation and TEM Imaging

Tissue samples of biopsies from endoscopically-normal rectal mucosa were acquired from 10 human subjects at the time of their colonoscopy in accordance with standard clinical practice. The colonoscopies indicated that five of these patients harbored precancerous adenomatous polyps in their colon. 50 TEM images (10 images/patient) of rectal tissues were obtained from these patients. The other five patients were found to be adenoma-free. 50 TEM images (10 images/patient) of rectal tissues were obtained from these patients, as well. All tissue samples went through the following steps: fixation, staining, embedding, sectioning, and finally TEM imaging, as per standard protocols (see Methods for details). It should be noted that all of the tissue samples in this study appeared to be normal when scrutinized using standard macroscopic and microscopic procedures.

(ii) Quantification of the nanoscale mass density fluctuations via IPR study

Figures 3*A* and 3*B* show representative TEM grayscale images of rectal tissue samples from adenoma-free patients and samples from patients harboring precancerous adenomatous polyps in their colon. Figures 3*C* and 3*D* show the corresponding IPR images (IPR pixel by pixel; IPR pixel dimension = 154 nm × 154 nm; lattice size = 20 × 20). The IPR images clearly

indicate two different disorder states for tissues from the normal and the early precancerous patients.

Figure 3*E* shows $< IPR(L) >_{\text{Pixel}}$ distributions for rectal tissues from the normal and the early precancerous patients for IPR pixel sizes $L \times L$ = 154 nm ×154 nm (i.e., lattice sizes $L_a = L/a$, a = 7 nm, $L_a \times L_a = 20 \times 20$). This figure illustrates a distinct separation in the IPR distributions between the two groups of patients. The average and standard deviation of the distributions both increase with the sample (i.e., lattice) size.

Figure 3*F* shows plots of $<< IPR(L) >_{\text{Pixel}} >$ versus L for three different cases: (i) uniform lattice; (ii) rectal tissues from the normal patients; and (iii) rectal tissues from the early precancerous patients. The ensemble averaging denoted by < > was performed over 500,000 IPR pixels for the IPR pixel length L = 77 nm (i.e., L_a = 10), and over 31,250 IPR pixels for the pixel length L = 308 nm (i.e., L_a = 40) for each group of patients. The value of $<< IPR(L) >_{\text{Pixel}} >$ for the uniform sample (i.e. background) increases with increased L, and then it saturates to a (universal) value of IPR ~ 2.5 at about the lattice size L_a = 40 (i.e., L = 308 nm, $N = 40 \times 40$).

The three curves in Fig. 3*F* clearly show that the $<< IPR(L) >_{\text{Pixel}} >$ value is highest for the rectal tissues from the early precancerous patients. For example, $<< IPR(L) >_{\text{Pixel}} >$ values for the uniform background, the normal-patient rectal tissues, and the early precancerous-patient rectal tissues are, respectively, ~2.5, 3.053, and 3.196. Higher values of the average IPR correspond to larger disorder strengths due to increased nanoscale fluctuations in the tissues. Figure 3*F* (inset) shows that values of the standard deviation $\sigma(< IPR(L) >_{\text{Pixel}})$ versus L for the early precancerous-patient rectal tissues are larger and increase faster than those of the normal-patient rectal tissues. Importantly, Fig. 3*F* also shows that the ratio $\sigma(< IPR(L) >_{\text{Pixel}})$ / $<< IPR(L) >_{\text{Pixel}} >$ increases much faster with increasing L for the early precancerous-patient rectal tissues relative to the normal-patient rectal tissues. The rapid increase of this ratio is attributed to the long tails in the IPR distributions.

Note that, due to the very large number of samples (e.g., for L = 308 nm, the number of samples or IPR pixels = 31,250), the results shown in Fig. 3 for our rectal-tissue study are highly statistically significant (Student t-test, two-tailed p-value = 5.95×10^{-38}).

Overall, the results shown in Fig. 3 provide substantial evidence that microscopically normal appearing colonic epithelial cells in early carcinogenesis exhibit more nanoscale disorder than the cells from a normal patient. This results suggest that IPR has the potential to detect early carcinogenic alterations in colon.

IV. Summary and Discussion

We have reported an IPR analysis technique to quantify the short-range light-localization properties of nanoscale mass-density fluctuations. We assumed a mean absorption coefficient of the tissue biomass for the TEM contrast agent, and linearity between TEM grayscale image fluctuations and the effective refractive-index fluctuations. These two assumptions are plausible for thin samples and for weak mass-density fluctuations.

We first showed that the IPR technique can be used to quantify minute changes in the nanoscale disordered dielectric media comprising a known or controlled-disordered model system which mimics a biological system, but in a much simpler way. This indicates that the IPR is an important parameter for quantifying nanoscale disorder.

We next applied IPR analysis to a controlled experimental study involving human colon cancer cells: the HT29 cell line, and its more aggressive (but cytologically indistinguishable) CSK genetic variant. We found that the IPR technique reveals that CSK cells have significantly larger nanoscale mass-density fluctuations than HT29 cells.

Finally, we found experimental evidence derived from human subjects for increased disorder of nanoscale refractive-index fluctuations (i.e., increased average IPR values) associated with histologically normal rectal mucosa located remotely from precancerous colon lesions. This evidence points towards the IPR technique being the first approach that enables quantifying the "Field effect" of colon carcinogenesis (17). Until now, no morphological alterations in the earliest stage of carcinogenesis have been reported. Only molecular (e.g., genetic, epigenetic, and proteomics) alterations have been described. The increase in the nanoscale disorder reported here using the IPR technique may represent the earliest morphological alteration in carcinogenesis known to-date.

We anticipate that IPR study of TEM images will have potential applications for tissue/cell characterizations in basic biological research, as well as medical applications in detecting early-stage cancers.

V. Methods

Preparation of dielectric nanoparticles and samples

Chemicals: Iron(III) acetylacetonate, dodecalamine, lauric acid, 1,2-hexadecanediol, Benzyl ether were obtained from Aldrich Chemicals and used without modifications.

Experimental: 6 to 7 nm size monodispersed nanoparticles were synthesized by simple chemical decomposition method in similar way as reported elsewhere. In the given protocol, Iron(III) acetylacetonate (2mmol) were used as a precursor to make Fe_3O_4 nanoparticles. Dodecalamine (6 mmol), lauric acid (6 mmol), and 1,2-hexadecanediol (10mmol) were added as capping agent as well as to control the size of the nanoparticles. Benzyl ether (20ml) was used as the solvent. The solution was heated to 200 C for 30 min then raised to 280° C for 30 min under inert atmosphere. Synthesized nanoparticles were washed with hexane, ethanol, and acetone to remove the unreacted chemical impurities.

Sample preparation: 1.25 mg/ml concentration of magnetite nanoparticles solution was prepared in hexane. This solution was drop-coated on carbon Type-A, 300 mesh copper grid, (hole size: 63 μm) and dried for 10 mins followed by 5 sec of ultrasonication.

Characterization: A Hitachi HF-8100 transmission electron microscope (TEM) was used to characterize the nanoparticles using the image mode. TEM grids were analyzed on the Hitachi HF8100 operated at an accelerating voltage of 200 kV.

HT29 and CSK cells

HT29 cells were grown in McCoy's medium mixed with 10% FBS mixed with 50 ug/mL Penicillin/streptomycin under 5% CO_2 environment at 37 degree Celsius. CSK shRNA vector (BD Biosciences- Clontech San Jose, CA) was transfected in HT29 cells by using Lipofectamine 2000 (Invitrogen, Carlsbad, CA) according to standard protocol given by the manufacturer. Transfected cells were then incubated at 37 degree Celsius in a humidified 5% CO_2 incubator. Stable clones for control vector were selected by puromycin (0.5μg/ml) while for CSK shRNA vector were selected by hygromycin (600μg/ml). Knockdown of the specific

gene for the stable clones was confirmed by RT-PCR and western blotting. Proteins from the stable constructs of CSK shRNA and control vector were isolated and subjected to western blotting using standard procedures and probed with antibodies against CSK (BD Biosciences) and PCNA (both from Santa Cruz Biotechnology) and beta actin (Sigma). It was found that stable transfection of the shRNA vectors resulted in 50% decrease in the expression of CSK. We have previously shown that CSK down-regulation leads to increased epithelial cellular proliferation (7,16). This was evidenced by a significant increase in the proliferation specific marker PCNA in the CSK shRNA construct. These procedures verified the aggressiveness of the CSK constructs.

TEM sample preparation and TEM imaging:

Cell and biopsy samples were first placed in Karnovsky's fixative for 2 weeks to preserve structure. The fixative consists of 0.1M phosphate buffered solution containing 5% glutaraldehyde and having a pH between 7.2 and 7.4. As per a standard protocol, the samples were stained with osmium tetraoxide (OsO_4), dehydrated and then embedded in resin containing 36% ERL 4221, 12% diglycidyl ether of polypropyleneglycol (DER 736), 51% nonenyl succinic anhydride (NSA), and ~1% dimethylaminoethanol (DMAE) by mass. Samples were then sectioned with an ultra-microtome to a thickness of 70nm and imaged with a 200 kV TEM machine.

Acknowledgement

Tissue samples were acquired in accordance to the Institutional Review Board (IRB) at NorthShore Unversity HealthSystems. This work was supported in part by NIH grants R01 EB003682 and R01 CA112315, and by NSF grant CBET-0733868. We also thank the Northwestern University TEM facilities for the TEM images, and our undergraduate research assistants for helping in collecting the samples.

References:

1. Femal A, Siegel R, Ward E, Hao Y, Xu J, Thun MJ (2009) Cancer statistics, 2009. *C Cancer J Clin.* 59:225-49.

2. Delcuve GP, Rastegar M, and Davie JR (2009) Epigenetic control (2009) *J Cell Physiol.* 21:243-250.

3. Mohn F and Schubeler D (2009) Genetics and epigenetics: stability and plasticity during cellular differentiation. *Trends Genet*.

4. Adams P D (2007) Remodeling of chromatin structure in senescent cells and its potential impact on tumor suppression and aging. *Gene* 397:84-93.

5. Zuckerkandl E and Cavalli G (2007) Combinatorial epigenetics, "junk DNA", and the evolution of complex organisms. *Gene* 390:232-42.

6. Lawlis SJ et al. (1996) Chromosome architecture can dictate site-specific initiation of DNA replication in Xenopus egg extracts. *J Cell Biol.* 135:1207-18.

7. Fox CA and Weinreich M (2008) Beyond heterochromatin: SIR2 inhibits the initiation of DNA replication. *Cell Cycle* 7:3330-3334.

8. Kanai Y and Hirohashi S (2007) Alterations of DNA methylation associated with abnormalities of DNA methyltransferases in human cancers during transition from a precancerous to a malignant state. *Carcinogenesis* 28: 2434-2442.

9. Elli RJ (2001) Macromolecular crowding: obvious but underappreciated. *TRENDS Biochem. Sci.* 26: 597-603.

10. Beuthany J, Minety O, Helfmannz J, Herrigz M and M¨ullerz G (1996) The spatial variation of the refractive index in biological cells. *Phys. Med. Biol.* 41:369–382.

11. Perelman LT, *et al.* (1998) Observation of periodic fine structure in reflectance from biological tissue: A new technique for measuring nuclear size distribution. *Phys Rev Lett* 80: 627–630.

12. Mourant JR, *et al.* (1995) Spectroscopic diagnosis of bladder cancer with elastic light scattering. *Laser Surg Med* 17:350–357.

13. Sokolov K, Drezek R, Gossage K, Richards-Kortum R(1999) Reflectance spectroscopywith polarized light: Is it sensitive to cellular and nuclear morphology. *Optics Express* 5:302–317.

14. Coffey D S (1998) Self-organization, complexity and chaos: The new biology for medicine. *Nat. Med.* 4: 882-885.

15. Born M, Wolf E (1999) *Principles of Optics: Electromagnetic Theory of Propagation, Interference and Diffraction of Light* (Cambridge Univ Press, Cambridge, UK).

16. Subramanian H, Pradhan P, Liu Y, Capoglu I, Li X, Rogers JD, Heiftez A, Kunte D, Roy HK, Taflove A, Backman V (2008) Optical Methodology for Detecting Histologically Unapparent Nanoscale Consequences of Genetic Alterations in Biological Cells. *Proc. Natl. Acad. Sci. USA* 105: 20124–20129 .

17. Subramanian H, Pradhan P, Liu Y, Capoglu I, Rogers JD, Roy HK, Brand RE and Backman V (2009) Partial wave microscopic spectroscopy detects sub-wavelength refractive index fluctuations: an application to cancer diagnosis. *Opt. Lett.* 34: 518-520.

18. Subramanian H, Roy HK, Pradhan P, Goldberg, Muldoon J, Brand RE, Sturgis C, Hensing T, Ray D, Bogojevic A, Mohammed J, Chang J-S and Backman V (2009) Nanoscale Cellular Changes in Field Carcinogenesis Detected by Partial Wave Spectroscopy. *Cancer Res.* 69: 5357 .

19. Bozzola JJ, Dee L (1999) *Electron Microscopy : Principles and Techniques for Biologists* (Jones and Bartlett).

20. Leapman RD (2006) Scanning Transmission Electron Microscope (STEM) Elemental Mapping by Electron Energy-Loss Spectroscopy. *Ann. NY Aca. Sci.* 483: 326-338.

21. Pradhan P and Sridhar S (2000) Correlations due to localization in quantum eigenfunctions of disordered microwave cavities. *Phys. Rev. Lett.* 8: 2360-2363.

22. Pradhan P and Sridhar S (2002) From chaos to disorder: Statistics of the eigenfunctions of microwave cavities. *Pramana J. Phys.* 48: 333-341.

23. Schwartz T, Bartal G, Fishman GS, and Segev M (2007) Transport and Anderson localization in disordered two-dimensional photonic lattices. *Nature* 446, 52-57

24. V.N. Prigodin and B.L. Altshular, Phys. Rev. Lett, **80** 1944 (1998) .

25. Kunte DP, Wali RK, Koetsier JL, Hart J, Kostjukova MN, Kilimnik AY, Pyatkin IG, Strelnikova SR, Roy HK (2005) Down-regulation of the tumor suppressor gene C-terminal Src kinase: an early event during premalignant colonic epithelial hyperproliferation. *FEBS Lett.* 579:3497-502.

26. Bernstein C, Bernstein H, Payne CM, Dvorak K, Garewal H (2008) Field defects in progression to gastrointestinal tract cancers. *Cancer Lett*. 260:1-10.

27. Dakubo, G.D., et al. (2007) Clinical implications and utility of field cancerization. *Cancer Cell Int.* 7: 2.

28. Zeitler E and Bahr GF (1962) A Photometric Procedure for Weight Determination of Submicroscopic Particles Quantitative Electron Microscopy. *J. Appl. Phys.* 33, 847-850

29. Loferer-Kröbβbacher M, Klima J, and Psenner R (1997) Determination of Bacterial Cell Dry Mass by Transmission Electron Microscopy and Densitometric Image Analysis. *Appl. and Environ. Microbiol.* 64, 688 .

30. Kramer B and MacKinnon A (1993) *Rep. Prog. Phys.* 56: 1469.

31. Schmitt JM and Kumar G (1996) Turbulent nature of refractive-index variations in biological tissue. *Opt. Lett.* 21: 1310-1312.

32. Lee PA and Fisher DS (1981) Anderson Localization in Two Dimensions. *Phys. Rev. Lett.* 47: 882 -885.

33. Prigodin VN and Altshular BL, *Phys. Rev. Lett,* 80: 1944-1947.

Figure Legends

Figure 1.

Top: Representative TEM micrograph of dielectric nanoparticles on dielectric film and corresponding discrete lattice.

Figs. 1*A*, 1*B* and 1*C* show the representative grayscale images of dielectric nanoparticles on dielectric thin films with increasing particle concentration (or disorder strength).

Figs. 1*D*, 1*E* and 1*F* are corresponding IPR images. Figs. 1*G*, 1*H* and 1*I* are the IPR_{Pixel} distributions corresponding to above IPR images, showing that the IPR distribution shifts to the higher values with more disorder. Fig. 1*J* shows $<IPR\_{Pixel}(L)>$ vs. L plots for uniform sample and three different disordered samples. The average value of IPR is more for stronger disorder for all length scales.

Figure 2.

Figs. 2*A* and *B* show representative TEM images of HT29 cell and CSK cells.

Figs. 2*C* and *D* corresponding IPR_{Pixel} images for L×L = 154×154 nm^2.

Fig. 2*E* shows relative $< IPR(L) >_{Pixel}$ distributions (ensemble averaged) of (i.e., IPR-pixel) sizes L×L = 154×154 nm^2 for HT29 and CSK cells.

Fig. 2*F* shows the ensemble average values $<< IPR(L) >_{Pixel} >$ versus *L* (in nm) plots for: (i) uniform sample (or background), (ii) HT29 cells, and (iii) CSK.

(Inset) Standard deviation $\sigma(< IPR(L) >_{Pixel})$ versus *L* (in nm) plots for HT29 cells and CSK cells.

Figure 3.

Figures 3*A* and *B*: Representative TEM images of tissues from normal patients and patients harboring colonic adenometous polyps.

Figs. 3*C* and *D*: Corresponding IPR-pixel images for the pixel lattice size 20×20 (154×154 nm^2).

Fig. 3*E* shows relative $< IPR(L) >_{Pixel}$ distributions (ensemble) of IPR-pixel sizes L×L = 154×154 nm^2 for normal rectal tissues from normal patients and early precancerous patients.

Fig. 3*F* shows the ensemble average values of the IPR-pixel $<< IPR(L) >_{Pixel} >$ versus *L* (in nm) plots for: (i) uniform background, (ii) normal tissues, and (iii) early precancerous tissues. (Inset) Standard deviation $\sigma(< IPR(L) >_{Pixel})$ versus *L* (in nm) plots for normal tissues and early precancerous tissues, corresponding to Figs. 3*A*-*B*.

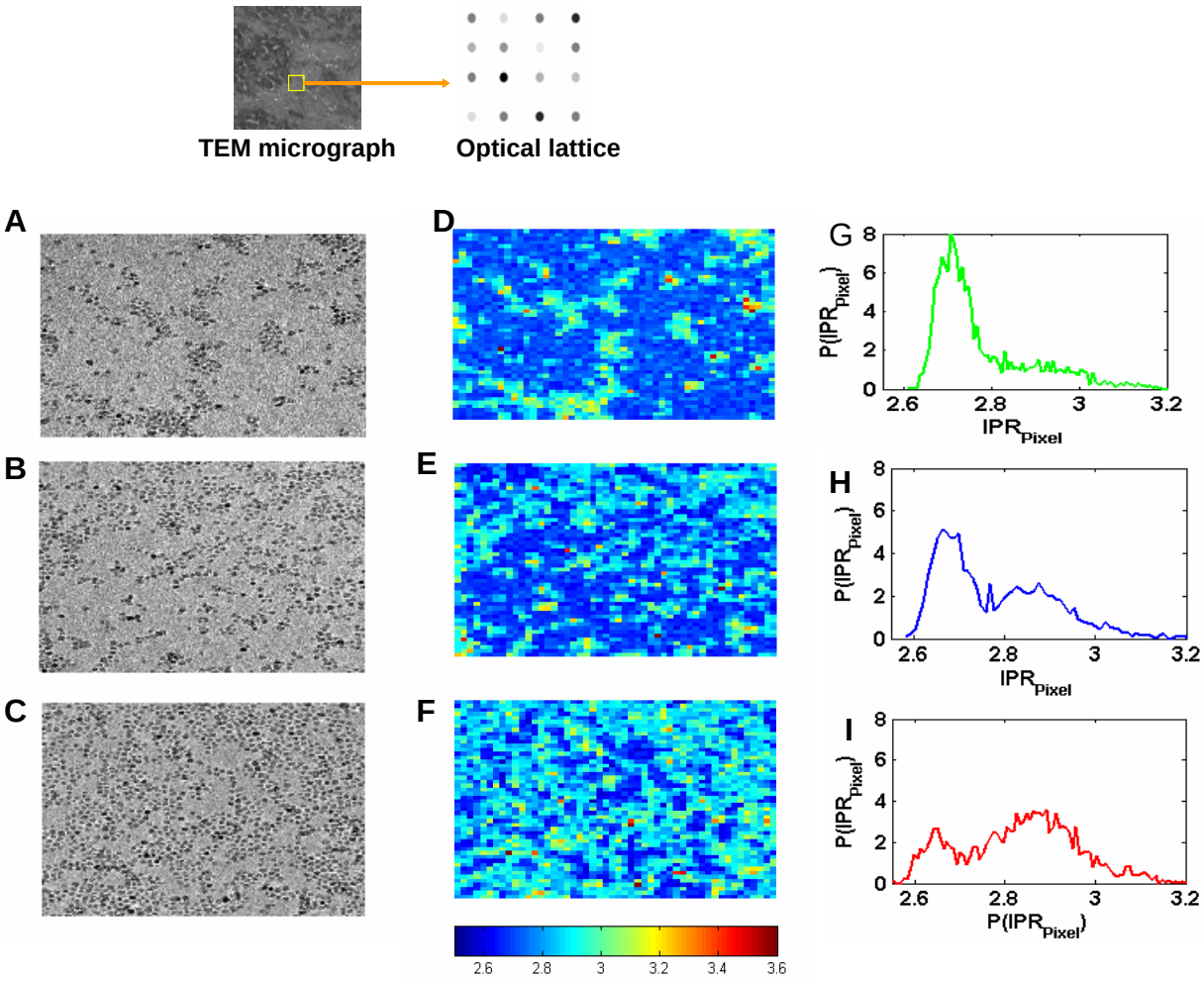
TEM micrograph
Optical lattice
A
B
C
D
E
F
G
H
I
J
2.6
2.8
3
3.2
3.4
3.6
P(IPR_Pixel)
IPR_Pixel
<<IPR>_Pixel>
Low conc
Medium conc
High conc
20
25
30
35
40
2.7
2.8
2.9
3
3.1
3.2
3.3

Figure 1

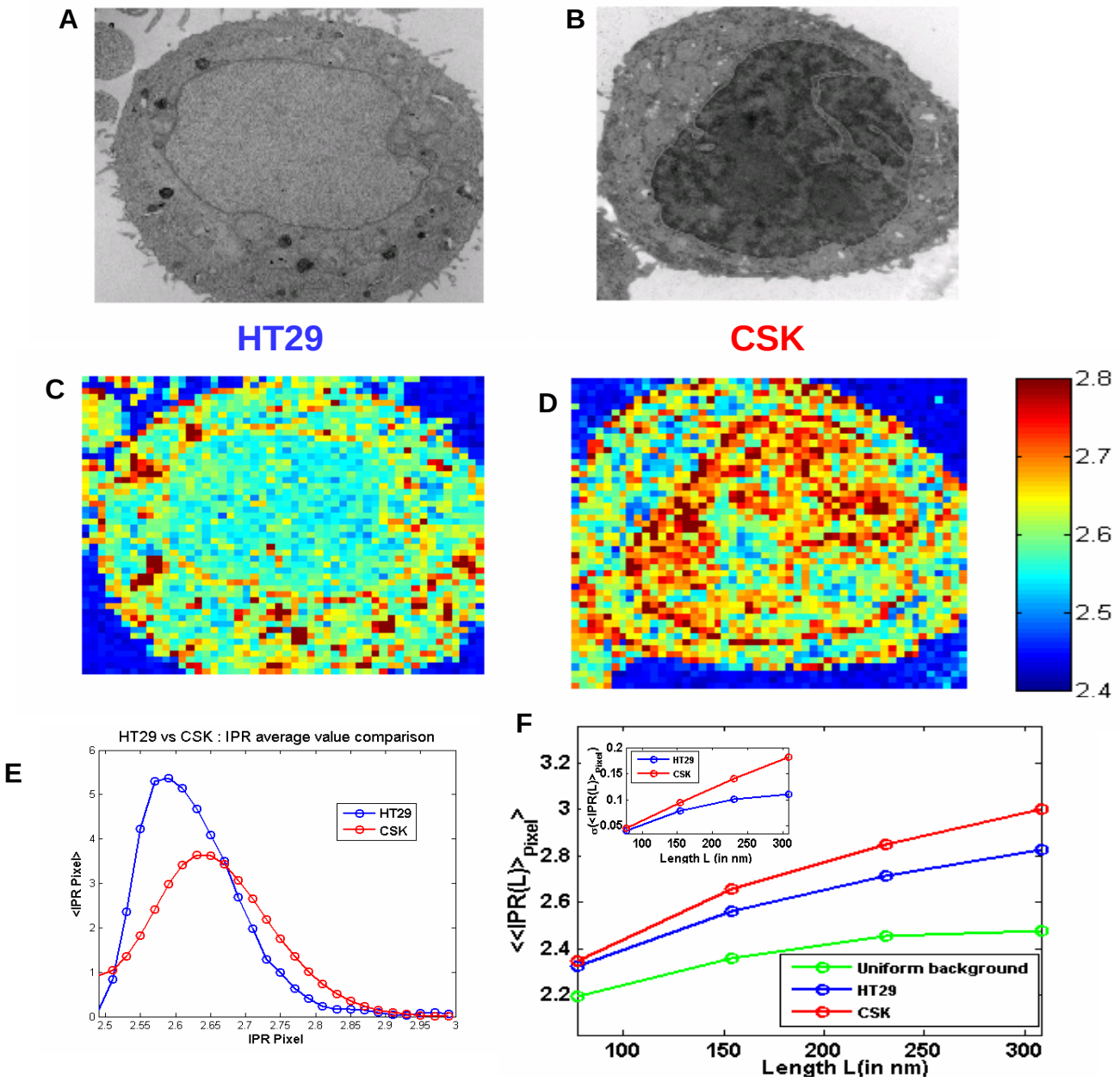
A
B
HT29
CSK
C
D
2.8
2.7
2.6
2.5
2.4
E
HT29 vs CSK : IPR average value comparison
<IPR Pixel>
IPR Pixel
HT29
CSK
F
<<IPR(L)>Pixel>
Length L(in nm)
Uniform background
HT29
CSK
σ(<IPR(L)>Pixel)
Length L (in nm)

Figure 2

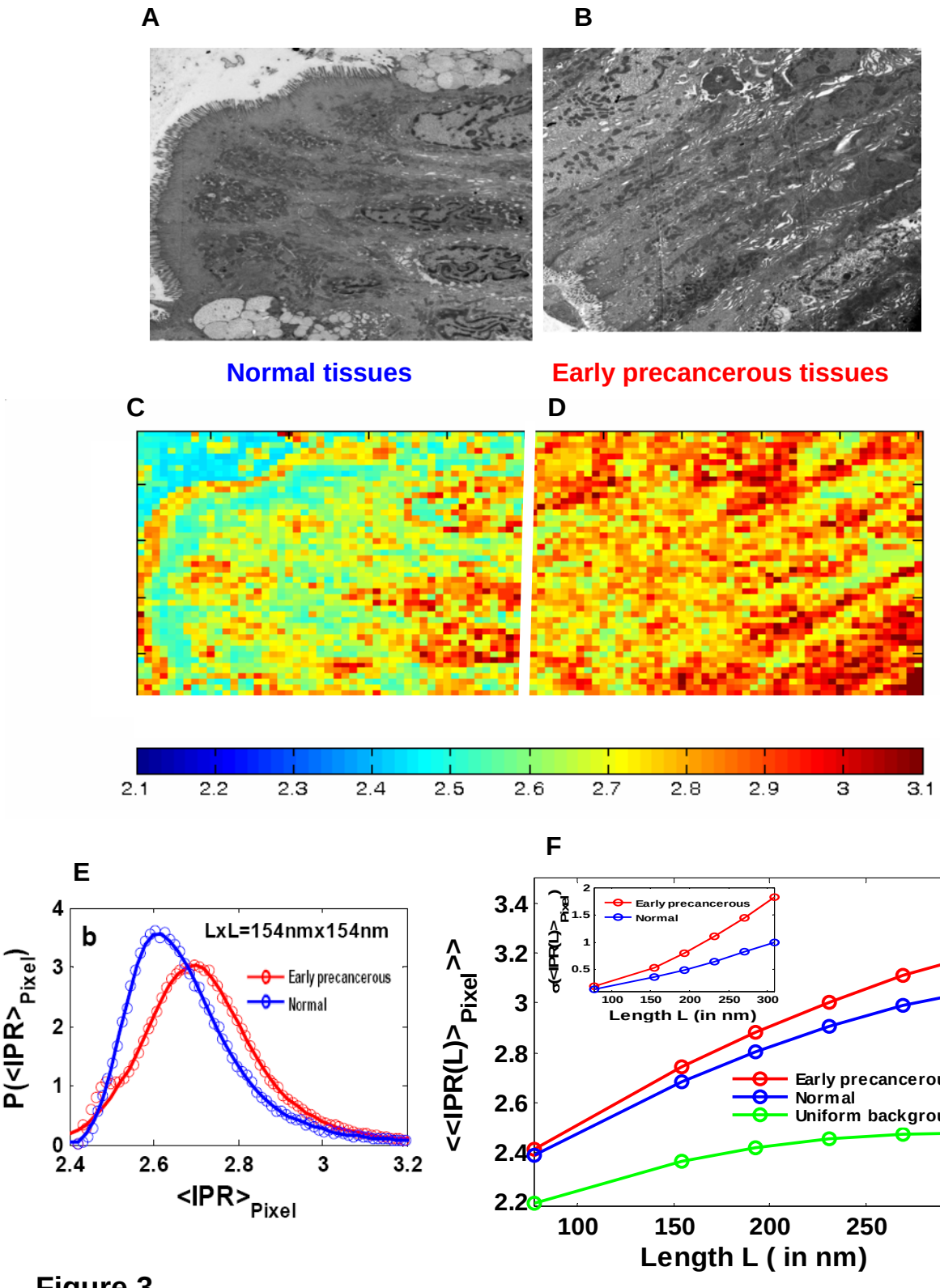
A
B
Normal tissues
Early precancerous tissues
C
D
2.1
2.2
2.3
2.4
2.5
2.6
2.7
2.8
2.9
3
3.1
E
b
LxL=154nmx154nm
Early precancerous
Normal
P(<IPR>Pixel)
<IPR>Pixel
F
<<IPR(L)>Pixel>>
Length L (in nm)
Early precancerous
Normal
Uniform background
σ(<IPR(L)>Pixel)
Length L (in nm)

Figure 3